Atomistic tight-binding theory of multiexciton complexes in a self-assembled InAs quantum dot

M. Zieliński,* M. Korkusiński, and P. Hawrylak
Institute for Microstructural Sciences, National Research Council, Ottawa, Canada K1A 0R6
(Received 20 August 2009; revised manuscript received 8 December 2009; published 1 February 2010)

We present atomistic tight-binding theory of electronic structure and optical properties of InAs/GaAs self-assembled quantum dots. The tight-binding model includes zincblende symmetry, faceting, and $sp^3d^5s^*$ atomic orbitals accounting for interband and intervalley couplings. The equilibrium positions of atoms are calculated using valence force field method and modification of the tight-binding Hamiltonian due to strain is accounted for using Harrison's law. The electronic and optical properties of multiexciton complexes are then determined by diagonalizing the many-body Hamiltonian for interacting electrons and holes using the configuration-interaction approach. The calculations of strain distribution approach 10^8 atoms while the electron and valence hole single-particle states are calculated by diagonalization of the Hamiltonian matrix with size on the order of 10^7. The dependence of predicted electronic and optical properties on InAs/GaAs valence-band offset and InAs absolute valence-band deformation potentials are described. The reliability of the atomistic calculations is assessed by comparison with results obtained from the effective bond orbital model and empirical pseudopotentials method.

DOI: 10.1103/PhysRevB.81.085301 PACS number(s): 73.21.La, 73.22.−f, 78.67.Hc, 71.15.−m

I. INTRODUCTION

Self-assembled quantum dots (SADs) (Refs. 1–3) involve millions of atoms and their electronic properties cannot at present be computed using *ab initio* methods, such as, e.g., GW-BSE approach.[4] Approximate methods, capturing atomistic structure of quantum dots and their matrix, include tight-binding[5–12] and pseudopotential[13–16] approaches. One of the approximate methods, valence force field-tight-binding-configuration interaction (VFF-TB-CI) discussed here, involves three steps:[5,6,11,17] (a) calculation of equilibrium position of constituent atoms using VFF model, (b) calculation of quasielectron and quasihole states (equivalent to the GW step) using a linear combination of atomic orbitals (LCAO) approach in a TB approximation, and (c) inclusion of final-state interactions by defining an effective Hamiltonian of interacting excited quasiparticles, diagonalized using the CI method. The approximate nature of such an approach requires careful analysis of results, and in particular an analysis of sensitivity of results to approximations made. Benefits include predictive capability allowing us to understand the dependence on size, geometry, composition, and external electric and magnetic fields of the electronic and optical properties of SADs.

In this paper we present results of the VFF-TB-CI methodology applied to InAs/GaAs SADs, with convergent strain distribution computed using the VFF approach for hundreds of millions of atoms, the electron and hole single-particle (SP) states computed using the 20-band $sp^3d^5s^*$ tight-binding model for millions of atoms, and energies, states, and emission spectra from up to ten exciton complexes obtained in the configuration-interaction method. In the VFF calculation we use the Keating model with material parameters derived from bulk elastic constants c_{ij}.[18] The TB parameters for unstrained InAs and GaAs are obtained by fitting of the TB bulk band edges and effective masses to those obtained in experiment or by *ab initio* calculations, with the valence-band offset (VBO) built into the parameter set.[17] The dependence of band edges on lattice deformation computed using density-functional theory (DFT) (Ref. 19) is used to find strain corrections to TB parameters. We generate two sets of parameters corresponding to two DFT results predicting opposite behavior of the valence-band edge. The Coulomb matrix elements needed for CI are obtained with TB wave functions involving $\sim 10^8$ orbitals, with on-site terms computed by approximating the TB basis with Slater orbitals. The interactions are screened by a distance-dependent dielectric function. In the CI step, typically $\sim 10^4$ configurations are used as a basis for each multiexciton system, while emission spectra are calculated from Fermi's golden rule.

We illustrate the method by computing the electronic and optical properties of a lens-shaped SAD. We find that in both cases the quasielectron states are organized in degenerate shells, a result independent of the VBO and strain parameters. The quasihole states are sensitive to these constants and do not reveal a shell structure for the lens-shaped dot. We study the signature of this sensitivity in multiexciton emission spectra. The reliability of the atomistic calculations is assessed by comparison with results obtained from the effective bond orbital model (EBOM) rooted in the $k\cdot p$ approximation and empirical pseudopotentials method of Zunger and co-workers.

The paper is organized as follows. Section II contains the definition of the geometry of the system. Next we discuss the details of the model, starting with the calculation of strain (Sec. III), the tight-binding model for electronic-structure calculation (Sec. IV) and the coupling of these two elements (Sec. V). Sections VI and VII discuss the resulting evolution of the bulk bands as a function of strain, and their sensitivity to the valence-band offset, respectively. In Sec. VIII we outline the calculations of the Coulomb and dipole matrix elements, while in Sec. IX we describe the computational procedure used to diagonalize the many-body Hamiltonian. Section X presents a detailed discussion of all aspects of our VFF-TB-CI computation on the example of a lens-shaped quantum dot. Finally, in Sec. XI we summarize the paper.

 ©2010 The American Physical Society

II. GEOMETRY DEFINITION

We start with InAs quantum dots embedded in GaAs. We define the size and shape of InAs quantum dot and embed the dot in a box of barrier GaAs material. In, As, and Ga atoms are placed on the sites of GaAs zincblende lattice. The dimension of the surrounding GaAs box defines the size of the computational domain.

The theory will be illustrated by calculations carried out for a lens-shaped quantum dot, for which results of EBOM and pseudopotential calculations are available. The height of the dot is $h=3.5$ nm and the base diameter is $D=25$ nm. The center of the base of the quantum dot is placed on the anion (As) atom. The dot is placed on one lattice constant (~ 0.6 nm) thick wetting layer.

III. ATOMISTIC CALCULATION OF STRAIN

There is a $\sim 7\%$ lattice mismatch between InAs and GaAs. The resulting strain is the driving force for the growth of self-assembled quantum dots. It also plays an important role in determining their electronic and optical properties. We use the approach in which the strain calculation process is equivalent to finding atomic positions that minimize the total elastic energy. At the same time the knowledge of atomic positions is a prerequisite for the atomistic calculation of the electronic structure.

In the continuous elasticity theory[20] the elastic energy is defined as a sum of local distortions of a continuous medium discretized on a computational grid. Unfortunately, this approach neglects atomistic details of interfaces and the lack of inversion symmetry of the zincblende lattice. Here, we use the atomistic approach of Keating,[21] in which the total elastic energy E_{TOT} contains the stretching and bending terms from each atomic bond

$$E_{TOT} = \frac{1}{2}\sum_{i=1}^{N}\sum_{j=1}^{\mathrm{nn}} A_{ij}[(\vec{R}_i - \vec{R}_j)^2 - d_{ij}^2]^2 + \sum_{i=1}^{N}\sum_{j=1}^{\mathrm{nn}}\sum_{k=j+1}^{\mathrm{nn}} B_{ijk}\left[(\vec{R}_j - \vec{R}_i)(\vec{R}_k - \vec{R}_i) - \frac{1}{3}d_{ij}d_{ik}\right]^2. \quad (1)$$

Here, $\vec{R}_i$ denotes the position of the ith atom, d_{ij} is the bulk bond length between the ith and jth atoms, and A_{ij} and B_{ijk} are material-dependent elastic parameters. The summations go over N atoms and nearest neighbors (nn). We start from a uniform lattice with GaAs lattice constant and to obtain strain field, we minimize total elastic energy with respect to the atomic positions using the conjugate gradient algorithm. The equilibrium positions of atoms are displaced from those in the bulk, and these displacements, i.e., the lengths and directions of atomic bonds, vary across the sample. As a measure of the displacement field, distribution of strain tensor elements across the sample is then computed by comparing the deformed zincblende unit cells with their unstrained bulk counterparts.[20]

Because strain is long ranged, the GaAs buffer (computational domain) used in the strain-energy minimization must be large enough to ensure that the strain fields vanish at the GaAs buffer boundaries. Lee *et al.*[22] investigated in detail the vertical size of the GaAs buffer needed to obtain vanishing hydrostatic strain at the box boundaries.

IV. ATOMISTIC TIGHT-BINDING ELECTRONIC-STRUCTURE CALCULATION

With the equilibrium atomic positions known, we can attempt to calculate the single-particle electronic structure of the system. The single-particle spectrum describes a quasiparticle moving in a field of atoms and dressed by interaction with all other electrons. The quasiparticle Hamiltonian in GW approximation reads[4]

$$\hat{H}_{QP} = \vec{p}^2/2m + V_{atomic}(\vec{r}) + V_{Hartree}(\vec{r}) + \Sigma(E,\vec{r}), \quad (2)$$

where $V_{atomic}(\vec{r})$ is the sum of atomic potentials, $V_{Hartree}(\vec{r})$ is the Hartree potential produced by all electrons, and $\Sigma(E,\vec{r})$ is the energy-dependent self-energy due to exchange and correlation. In the density-functional approximation the self-energy is replaced by the exchange-correlation potential. If we were able to carry out fully self-consistent density-functional calculations, the Kohn-Sham Hamiltonian would have been expressed in terms of atomic, Hartree, and exchange-correlation potentials, themselves functionals of electronic density. Since we do not know the Hamiltonian, we parametrize it in a tight-binding form by first expanding the wave function in a basis of atomic orbitals

$$\phi = \sum_{\vec{R},\alpha} c_{\vec{R}\alpha}|\vec{R}\alpha\rangle, \quad (3)$$

and next forming the Hamiltonian matrix in the atomic basis. By comparison, in a pseudopotential approach[13–16] the atomic, Hartree, and self-energy potentials are replaced by a sum of effective atomic potentials. These atomic potentials are next used to generate one-electron potential of the nanostructure.

In our tight-binding approach the wave function on each atom is described by ten valence orbitals for each spin: one of type s, three of type p, five of type d, and an additional s^* orbital that accounts for higher lying states. Each orbital is doubly spin degenerate, thus resulting in a total of 20 bands. The resulting Hamiltonian of quasiparticle in an N-atom quantum dot, written in the language of second quantization, reads

$$\hat{H}_{\mathrm{TB}} = \sum_{i=1}^{N}\sum_{\alpha=1}^{20}\epsilon_{i\alpha}c_{i\alpha}^{+}c_{i\alpha} + \sum_{i=1}^{N}\sum_{\alpha=1,\beta=1}^{20}\lambda_{i\alpha,\beta}c_{i\alpha}^{+}c_{i\beta} + \sum_{i=1}^{N}\sum_{j=1}^{4}\sum_{\alpha,\beta=1}^{20} t_{i\alpha,j\beta}c_{i\alpha}^{+}c_{j\beta}, \quad (4)$$

where $c_{i\alpha}^{+}(c_{i\alpha})$ is the creation (annihilation) operator of a carrier on the orbital α localized on the site i, $\epsilon_{i\alpha}$ is the corresponding on-site energy, and $t_{i\alpha,j\beta}$ describes the hopping of the particle between orbitals on neighboring sites. Coupling to farther neighbors is neglected. Finally, $\lambda_{i\alpha,\beta}$ accounts for the spin-orbit interaction by introducing finite matrix ele-

ments Δ connecting p orbitals of opposite spin, residing on the same atom, following the description given by Chadi.[23] For example, $\langle p_y,\uparrow|H|\downarrow,p_z\rangle=-i\Delta$. Spin-orbit-type coupling between d-type orbitals is neglected. Here we assume that each site holds 20 orbitals and is surrounded by four neighbors.

Hopping, i.e., off-diagonal matrix elements of our Hamiltonian are calculated according to the recipe given by Slater and Koster.[24] In this approach the hopping matrix elements $t_{i\alpha,j\beta}$ are expressed as geometric functions of two-center integrals and depend only on the relative positions of the atoms i and j. Contributions from three-center and higher integrals are neglected. For example, if the two atoms are connected by a bond along the x axis then orbitals s and p_z create a π bond and the matrix element $t_{s,p_z}=V_{s,p_z\pi}=0$ vanishes because of the symmetry. On the other hand, if the direction of the bond is along y axis, i.e., vertical, then the bond is of a σ type and $t_{s,p_z}=V_{s,p_z\sigma}$ is finite. In the general case the nearest neighbors are connected by bonds of any direction $\vec{d}=|d|(l\hat{x}+m\hat{y}+n\hat{z})$, with d being the bond length and l, m, n—the direction cosines. Then the tunneling t_{s,p_z} element can be expressed in terms of projecting the p_z orbital onto the bond and in the direction perpendicular to it. Since the perpendicular projections give π-type bonds, their contribution is zero. The Hamiltonian matrix element is thus $t_{i,s,j,p_z}=nV_{sp\sigma}$. Similar sets of rules are defined for all other t-matrix elements.[24]

This approach reduces the number of unknown matrix elements as they can be related via Slater-Koster rules to a relatively small subset of two-center integrals $V_{\alpha\beta,\gamma}$. This is particularly useful within the framework of empirical tight binding, where E_α, $\lambda_{\alpha,\beta}$, and $V_{\alpha\beta,\gamma}$ parameters are not directly calculated, but rather obtained by fitting[25] the TB bulk model results to experimentally known band gaps and effective masses at high-symmetry points of the Brillouin zone. We want to stress here that we are fitting TB model not only to bulk properties at Γ point, but also at X and L points to account for multivalley couplings.

The most frequent parameterizations used so far are given in Refs. 17, 18, and 26. These previous works demonstrated that the inclusion of d orbitals in the basis allows to obtain much better fits of the masses and energy gaps to the target material values. In particular, the treatment of the conduction-band edge is significantly improved, which is important for small nanostructures.[27] In this work we use our own parameterization, analogous to work by Klimeck *et al.*,[17] but giving better agreement with target bulk properties. More details will be presented in our future work.

In order to address the treatment of the interface between InAs and GaAs we note that this two materials share the same anion (arsenic). Thus during the fitting procedure diagonal matrix elements on arsenic are kept the same in both materials. This approach removes the necessity of averaging on-site matrix elements for interface atoms. Additionally, to account for the BO between the materials forming the interface, fit for InAs is performed in such a way that it includes band offset, i.e., the top of the valence band of InAs is set to be equal to the band offset value. This removes the necessity of shifting values of diagonal matrix element for interface atoms, which would result in two different sets of parameters for arsenic: one for InAs and another for GaAs. We analyze the importance of the choice of the VBO in Sec. X.

Finally, there is a second type of interface that arises on the edges of the computational box. There, the appearance of free surfaces leads to the existence of dangling bonds. Their presence results in spurious surface states, with energy inside of the gap of the barrier material, making it difficult to distinguish spurious states from the single-particle states of the quantum dot. A dangling-bond-energy shift that mimics the passivation procedure, described in Ref. 21 is performed in order to shift the energies of surface-localized states away from the energies corresponding to confined QD orbitals.

Finally, a parallel Lanczos diagonalizer with Kramers symmetry is used to resolve the Kramers-degenerate doublets. We performed a systematic study (similar to the one in Ref. 22) of the effect of the size of the tight-binding computational domain on the convergence of energies and wave functions of states confined in a quantum dot. This allowed us to ensure that the TB domain is large enough so that further extension of the computational box would change the single-particle energies by less then a small fraction of millielectron volt. Because the computational domain necessary for the converged tight-binding calculation involves (case-dependent) $\approx$1 million atoms, resulting tight-binding matrices are very large, i.e., ($\approx$20 million by 20 millon). This presents a significant numerical problem, but utilizing matrix sparsity, parallel computer and the fact that we need only several lowest electron and hole states, and not the entire Hamiltonian eigenspectrum, we achieved linear scaling as a function of the number of atoms.

V. INCLUSION OF STRAIN INTO TIGHT-BINDING HAMILTONIAN

As mentioned above, tight-binding parameters are obtained by fitting the bulk TB band structure to experimentally measured band structure of the unstrained bulk semiconductors. Since strain changes bond angles and lengths, the Hamiltonian matrix elements change as well. The Slater-Koster approach is particularly convenient in introducing the strain effects into the model since changes in bond angles are taken into account by the set of rules involving direction cosines.

To account for changes in bond lengths we use a generalized version of Harrison law:[28] $V_{\alpha\beta,\gamma}=V^0_{\alpha\beta,\gamma}(d_{ij}/d_0)^\eta$, where $V^0_{\alpha\beta,\gamma}$ is two-center integral for the unstrained case, d_{ij}/d_0 is the ratio of the new to old (ideal) bond length d scaled by the exponent η, value of which will be discussed later. Modified $V_{\alpha\beta\gamma}$ are used to build tight-binding Hamiltonian for the strained system.

Boykin *et al.*[18] argued that because tight-binding orbitals are not true atomic orbitals, but rather they are the orthogonalized Löwdin orbitals, the diagonal matrix elements might, in principle, also vary in response to displacements of neighboring atoms. Similarly, Jancu *et al.*[26] introduced uniaxial strain-induced splitting of otherwise degenerate d_{xy}, d_{yx}, and d_{zx} levels. These authors claim that uniaxial strain induces a tetragonal crystal field which lifts the degeneracy of the d atomic levels.

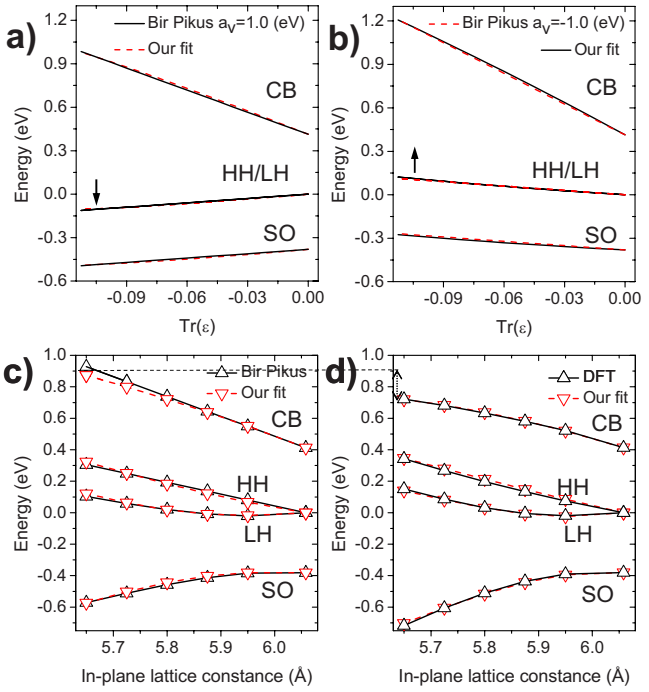

FIG. 1. (Color online) InAs band edges as a function of the hydrostatic deformation $\mathrm{Tr}(\epsilon)$ as calculated with our tight-binding model fitted to reproduce Bir-Pikus model for two different values of valence band absolute deformation potential (a) $a_v=1.0$ and (b) $a_v=-1.0$. InAs band edges under biaxial strain as calculated with our model fitted to reproduce (c) Bir-Pikus model ($a_v=-1.0$ eV) and (d) DFT calculation ($a_v=-0.88$ eV).

To summarize, both models include modification of on-site (diagonal) matrix elements due to strain, and we follow the model developed by Klimeck as it is more general and not limited to the case of the uniaxial strain. In this approach we have

$$\epsilon_{\vec{R}\alpha} = \epsilon^0_{\vec{R}\alpha} + \sum_{\vec{R}\in nn}\sum_{\beta} C_{\vec{R}\alpha,\vec{R}'\beta}\frac{t^0_{\vec{R}\alpha,\vec{R}'\beta} - t'_{\vec{R}\alpha,\vec{R}'\beta}}{\epsilon^0_{\vec{R}\alpha} + \epsilon^0_{\vec{R}'\beta}}, \tag{5}$$

where C are empirical material parameters, yet to be determined.

VI. BAND EVOLUTION AS A FUNCTION OF STRAIN

In the original work by Harrison,[28] η was assumed to be the same for all integrals $V_{\alpha\beta,\gamma}$. It was also determined to be equal to 2.0 by comparison of the TB model with the nearly free-electron model. In this work we fit the parameters η and C to match evolution of bulk band edges given by the Bir-Pikus (BP) model[29] with experimentally measured deformation potentials for the case of hydrostatic strain. However, we note that there is ongoing discussion[30–32] in literature regarding the sign of the absolute hole band deformation potentials a_v, both for InAs and GaAs. Henceforth we compare the results obtained using positive and negative values of a_v.

Figures 1(a) and 1(b) show evolution of InAs band edges as a function of hydrostatic deformation given as $\mathrm{Tr}(\epsilon)$, where ϵ is the hydrostatic strain tensor as calculated with our tight-binding model fitted to reproduce the Bir-Pikus model[29] for two different values of absolute valence-band deformation potential, (a) $a_v=1.0$ and (b) $a_v=-1.0$. In this model, for purely hydrostatic strain, the light and heavy holes remain degenerate and the evolution of the top of the valence band is given as

$$E_v = E_v^0 + a_v\,\mathrm{Tr}(\epsilon), \tag{6}$$

where E_v^0 is unstrained bulk top of the valence band.

Arrows denote different trend of the heavy/light hole band evolution as a function of compressive strain. The a_v parameter is important for confined system as it determines whether the confining potential for holes becomes deeper or shallower under hydrostatic strain. We note that other authors used both positive a_v (Ref. 20) and negative a_v (Ref. 15) in their calculation.

The strain in self-assembled quantum dots is not purely of hydrostatic kind, there is also a significant biaxial strain contribution. For the more complicated case of the biaxial strain we fit the tight-binding model to reproduce results obtained by both the Bir-Pikus model, and more elaborate DFT.[19]

Additionally, after the VFF strain relaxation, the in-plane lattice distances ("constants") in the wetting layer and in the quantum dot itself are strongly distorted from InAs bulk equilibrium value, almost matching that of GaAs. Because of this it is important to fit TB Hamiltonian to reproduce not only the evolution of band edges for small deformation (deformation potentials) but also band trends in a wide range of deformation.

Figures 1(c) and 1(d) show the evolution of InAs band edges under biaxial strain as calculated with our model fitted to reproduce (c) Bir-Pikus model (with $a_v=-1.0$) and (d) DFT calculation[33] ($a_v=-0.88$). We were able to achieve a much better fit to DFT than to the simple Bir-Pikus case, as Bir-Pikus model, compared to DFT, overestimates the energy evolution of the bottom of conduction band by almost 0.2 eV (dashed line). Such a difference will result in a similar, significant differences of energies of confined quantum dot states as described later on.

In order to combine both hydrostatic and biaxial strain in one set of parameters we developed a genetic algorithm that performs simultaneous fit to hydrostatic and biaxial strain cases.[34] In the later part of the work we will analyze the properties of electron and hole states as a function of different strain coupling methods.

VII. VALENCE-BAND OFFSET

Apart from the uncertainty of the sign of the absolute InAs (GaAs) valence-band deformation potential there is also a considerable spread in the values reported for the InAs/GaAs valence-band offset.[35,36] The reported values vary from 60 to 330 meV. Although specific choice of VBO will not affect the effective QD gap significantly,[10] large differences between extreme VBO values, combined with uncertainty of a_v, may correspond to a very different confining potential profile for the hole states depending on the choice of parameters. In this work we will study these problems by

using two different band offset values: VBO=210 meV as "recommended" by Ref. 35 and consistent with Ref. 36 and VBO=60 meV obtained by Wei and Zunger[30] and used by Zunger and co-workers in their empirical pseudopotential calculations.[15,16]

VIII. COULOMB AND DIPOLE MATRIX ELEMENTS

Once single-particle energy states are found, the next step is the calculation of many-body states of excited electrons and holes populating single-particle levels. The interaction of electrons and holes and their interaction with light requires calculation of Coulomb and dipole matrix elements.

In a GW approach one calculates the effective interaction W self-consistently. Not being able to carry out this calculation, we assume a statically screened Coulomb interaction. Hence the Coulomb matrix elements V_{ijkl} are given by

$$V_{ijkl} = \int\int \phi_i^*(\vec{r}_1)\phi_j^*(\vec{r}_2)\frac{e^2}{\epsilon(\vec{r}_1,\vec{r}_2)|\vec{r}_1-\vec{r}_2|}\phi_k(\vec{r}_2)\phi_l(\vec{r}_l), \tag{7}$$

where $\epsilon(\vec{r}_1,\vec{r}_2)$ is the position-dependent dielectric function, ϕ are single-particle wave functions obtained by diagonalization of the tight-binding Hamiltonian and given as LCAO

$$\phi_i = \sum_{\vec{R},\alpha} c^i_{\vec{R}\alpha}|\vec{R}\alpha\rangle. \tag{8}$$

If we substitute ϕ_i in this LCAO form into the formula (7), we get

$$V_{ijkl} = \sum_{\vec{R}_1\alpha_1}\sum_{\vec{R}_2\alpha_2}\sum_{\vec{R}_3\alpha_3}\sum_{\vec{R}_4\alpha_4} c^{i*}_{\vec{R}_1\alpha_1}c^{j*}_{\vec{R}_2\alpha_2}c^{k}_{\vec{R}_3\alpha_3}c^{l}_{\vec{R}_4\alpha_4} \times\langle\vec{R}_1\alpha_1,\vec{R}_2\alpha_2|\frac{e^2}{\epsilon(\vec{r}_1,\vec{r}_2)|\vec{r}_1-\vec{r}_2|}|\vec{R}_3\alpha_3,\vec{R}_4\alpha_4\rangle. \tag{9}$$

In the sums we separate out the onsite terms ($\vec{R}_1=\vec{R}_2=\vec{R}_3=\vec{R}_4$) and use for them the unscreened Coulomb interaction with dielectric constant $\epsilon=1$. In the remaining terms we take the Coulomb interaction screened by the bulk dielectric constant. In the derivation we take into account only two-center contributions (i.e., $\vec{R}_1=\vec{R}_4$ and $\vec{R}_2=\vec{R}_3$) and assume that for sites which are far apart the exact structure of the localized orbitals is not important[7] (i.e., in the integral we set $\vec{r}_1=\vec{R}_1$ and $\vec{r}_2=\vec{R}_2$). As a result we obtain an approximate form of Coulomb matrix elements

$$V_{ijkl} = \sum_{\vec{R}_1}\sum_{\vec{R}_2\neq\vec{R}_1}\left[\sum_{\alpha_1} c^{i*}_{\vec{R}_1\alpha_1}c^{l}_{\vec{R}_1\alpha_1}\right]\left[\sum_{\alpha_2} c^{j*}_{\vec{R}_2\alpha_2}c^{k}_{\vec{R}_2\alpha_2}\right]\frac{e^2}{\epsilon|\vec{R}_1-\vec{R}_2|} + \sum_{\vec{R}_1}\sum_{\alpha_1\alpha_2\alpha_3\alpha_4} c^{i*}_{\vec{R}_1\alpha_1}c^{j*}_{\vec{R}_1\alpha_2}c^{k}_{\vec{R}_1\alpha_3}c^{l}_{\vec{R}_1\alpha_4} \times\langle\vec{R}_1\alpha_1,\vec{R}_1\alpha_2|\frac{e^2}{|\vec{r}_1-\vec{r}_2|}|\vec{R}_1\alpha_3,\vec{R}_1\alpha_4\rangle. \tag{10}$$

The first term is the long-range contribution to the two-center integral built from the monopole interaction of two charge densities localized at different atomic sites. The second term is the on-site unscreened part, calculated by direct integration using atomic orbitals. As a first step, following Refs. 8 and 9 we model the tight-binding orbitals with atomic Slater orbitals. This approximation does not account for the monopole-dipole and dipole-dipole contributions,[37] which will be investigated in the future in relation with electron-hole exchange interactions.

In the calculation of Coulomb matrix elements we approximate LCAO basis orbitals by Slater orbitals. Lee *et al.*[8] investigated different orbitals, including nonorthogonal Slater and both nonorthogonal and orthogonalized Gaussian-type orbitals. The authors found the dependence of the results on the choice of basis orbitals decreasing quickly with the increasing dot size. They found that for the radius larger than $\approx$1.5–2 nm, and much smaller then dot investigated in this work, Coulomb interactions can be calculated reliably using the simple approximate orbitals as basis.

Dipole matrix element for light polarized along x direction are calculated by the following formulas:[7,38]

$$\langle\phi_e|x|\phi_h\rangle = \sum_{\vec{R}\alpha} R_x c^{e*}_{\vec{R}\alpha}c^{h}_{\vec{R}\alpha} + \sum_{\vec{R}\alpha}\sum_{\beta\neq\alpha} c^{e*}_{\vec{R}\alpha}c^{h}_{\vec{R}\beta}\langle\alpha|x|\beta\rangle + \sum_{\vec{R}_1\alpha}\sum_{\vec{R}_2\neq\vec{R}_1\beta} c^{e*}_{\vec{R}_1\alpha}c^{h}_{\vec{R}_2\beta}\langle\vec{R}_1\alpha|x|\vec{R}_2\beta\rangle, \tag{11}$$

where the first sum gives the "volume" contribution built from the atomic position dipole moments determined by the position of atom $\vec{R}=(R_x,R_y,R_z)$. The second term is built from intra-atomic dipole moments for atomic transitions between orbitals on the same atom and the last term collects contributions coming from orbitals centered on different atoms. As in the case of Coulomb matrix element we use Slater orbitals[27] to calculate intra-atomic and interatomic dipole elements.

IX. MULTIEXCITON HAMILTONIAN

Once the single-particle eigenstates ϕ_i, their energies E_i, and Coulomb matrix elements V_{ijkl} are found, the Hamiltonian for the interacting electrons and holes can be written in second quantization as[1]

$$\hat{H}_{ex} = \sum_i E^e_i c^\dagger_i c_i + \sum_i E^h_i h^\dagger_i h_i + \frac{1}{2}\sum_{ijkl} V^{ee}_{ijkl}c^\dagger_i c^\dagger_j c_k c_l + \frac{1}{2}\sum_{ijkl} V^{hh}_{ijkl}h^\dagger_i h^\dagger_j h_k h_l - \sum_{ijkl} V^{eh,dir}_{ijkl}c^\dagger_i h^\dagger_j h_k c_l + \sum_{ijkl} V^{eh,exchg}_{ijkl}c^\dagger_i h^\dagger_j c_k h_l. \tag{12}$$

We note that this Hamiltonian does include vertex corrections in the form of electron-hole interaction, but self-energy corrections are included indirectly in the electron and hole energies fitted to experimental transitions of bulk material. The investigation of self-energy correction will be carried out in the future.

Multiexciton configurations are built from several electron and hole single-particle states. We take into account six lowest electron and six hole levels, but each level corre-

sponds to doublet of two Kramers degenerate states giving a total of 12 electron and 12 holes states. The multiexciton wave function is expanded in terms of these configurations, the Hamiltonian matrix constructed in configuration space and diagonalized giving energies of ground and excited states of multiexciton complexes. As number of possible many-body configurations grows factorially with number of particles, in exact diagonalization approach we introduce a cutoff in number of configurations used in calculation. However, we make sure that analyzed features both in energy and optical spectra are converged with respect to the number of configurations and single-particle states used in building configurations.

Finally, the optical spectra are found by calculating the intensity of photoluminescence from the recombination of one electron-hole pair in a N-exciton state using Fermi's golden rule

$$I(\omega) = \sum_f |\langle f, N-1|P^-|i,N\rangle|^2 \delta(E_i - E_f - \hbar\omega), \qquad (13)$$

where $|i,N\rangle$ is ith state of the N-exciton system. The operator P^- describes all the possible electron-hole recombination channels

$$P^- = \sum_{lm} \langle l_e|\vec{\epsilon}\cdot\vec{r}|m_h\rangle c_l h_m, \qquad (14)$$

where $\langle l_e|\vec{\epsilon}\cdot\vec{r}|m_h\rangle$ is a dipole matrix element calculated from single-particle tight-binding wave functions for a given polarization of light $\vec{\epsilon}$.

X. RESULTS

A. Single-particle levels

We present here the results of calculations for a lens-shaped InAs dot, shown in Fig. 2(a). The height of the lens is $h=3.5$ nm and the base diameter is $D=25$ nm. We chose this particular size and shape to be able to compare our results with results of a different atomistic methodology, namely, empirical pseudopotentials (Refs. 15 and 16).

Figure 2(b) shows charge distributions and energies corresponding to several lowest electron and hole levels. In the atomistic calculation, due to the underlying zincblende lattice, the rotational symmetry C_∞ is reduced to C_{2v}, despite the cylindrical shape of the dot. As a result, the electronic states can no longer be labeled as eigenstates of angular momentum L_z, which is not a good quantum number. In principle, one should label states by different irreducible representations of the "crystal+dot" symmetry group, but for clarity and simplicity one can still label states approximately as of s, p, or d character by analysis of their nodal structure in real space. This approach works very well for electron states, which can be well described by single-band model and have well-defined directional and nodal properties. Therefore the ground electron state e_1 is of s symmetry with no nodal plane (Fig. 2), while the first and second excited states (e_2 and e_3) are of p symmetry, with one nodal plane each. First of the p states is localized along [110] crystal direction while the second p is localized perpendicularly

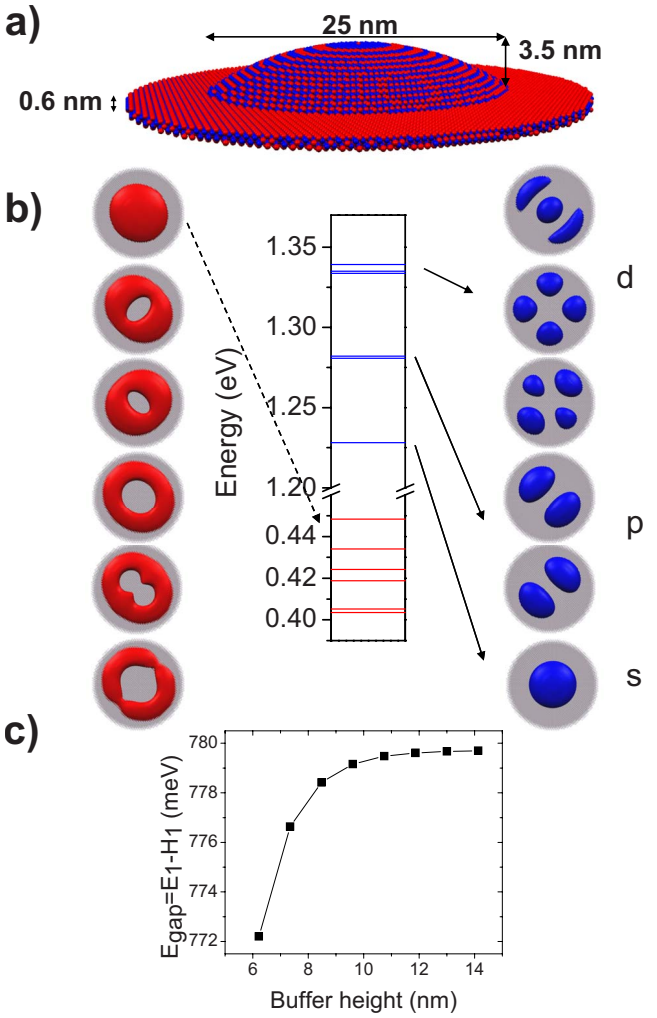

FIG. 2. (Color online) (a) Lens-shaped quantum dot embedded in GaAs (only indium and arsenic atoms are shown). (b) Electron (right) and hole (left) probability density isosurfaces and energies for dot (a). (c) Single-particle effective gap $E_{gap}=E_1-H_1$ as a function tight-binding computational domain height for dot (a).

along the [1$\underline{1}$0] crystal direction. This localization and elongation, also visible for other states, is due to underlying lattice symmetry and is enhanced further by strain effects.

The next three excited electron states have a more complicated nodal structure. Two of them, e_4 and e_5, can be denoted as $d_{x^2-y^2}$ and d_{xy} as they have two nodal planes on the xy plane. Above these states of d symmetry there is an e_6 state of approximate d (or $2s$) symmetry. This state has one node along radial coordinate, thus index 2 in contrast to the nodeless $1s$ state. In the effective-mass model with parabolic confinement the state corresponding to e_6 would be accidently degenerate with the d levels, forming a shell, while in atomistic calculation for self-assembled quantum dots all degeneracies (apart from Kramers) are removed.

The effective gap between electron and hole ground levels is 0.7797 eV, which is a reasonable value for pure (nonalloyed) InAs dot. Spacing between ground (s-type) and first excited (p-type) electron level is 52.7 meV, while the splitting of first and second excited (p-type) states is 1.28 meV. Spacing between the higher of two p-states and the lowest of

d states is 51.7 meV, and is very similar to that between ground and first excited states, thus very close to the prediction given by harmonic oscillator model, with the overall shell structure being very well preserved.

However, the structure of hole levels is different then those of electrons, more complicated due to the mixing of angular momenta and anisotropic effect of strain. Surprisingly, the hole energy levels cannot be grouped into quasidegenerate shells. Yet, the structure of lower hole levels charge densities is similar to those of electrons, with the ground hole h_1 state of s symmetry and the two first excited states of approximate p symmetry. Note that the first excited hole state h_2 is elongated along $[1\underline{1}0]$, perpendicular to the elongation axis of the first excited electron level e_2.

The energy difference between the ground and excited hole states is 14.4 meV, approximately one third of the corresponding value for electrons. Smaller spacings between hole levels in self-assembled quantum dots can be attributed to higher effective mass of holes. On the contrary, the splitting between p-type excited hole states h_2 and h_3 is 9.8 meV, is much larger then for electrons and comparable with energy difference between s and p. Large splitting of the p levels can be understood in terms of different biaxial strain contribution along [110] and $[1\underline{1}0]$ axes. It affects holes only as electrons, built predominantly from atomic s orbitals, are virtually immune, at least in the simplest Bir-Pikus model, to biaxial strain.

The higher lying state h_4 does not show a clear symmetry character, with spacing between h_3 and h_4 equal only 5.5 meV. However, two higher lying states h_5 and h_6 are well separated (13.5 meV) from h_4 and form a well-defined doublet with small, 1.8 meV, splitting. While the shell structure of holes is not visible in lens-shaped dots, Indium flush technique,[39] which creates thinner, more disklike dots leads to a hole shell structure[11] observed experimentally.[40]

B. Dependence of electron levels on valence-band offset and deformation potential

Figure 3 shows energies corresponding to several lowest electron (blue) and hole (red) levels obtained for different values of InAs/GaAs valence-band offset (VBO), different absolute InAs (GaAs) valence-band deformation potential a_v, and different models, BP or DFT, used in fitting tight-binding Hamiltonian to reproduce strained bulk band edges.

Different choice of VBO results in a simultaneous shift of the depth of both strained and unstrained electron and hole confining potentials. The bigger the VBO the deeper the well for holes and the shallower the well for electrons. However, the energy difference between the top of the valence band and the bottom of the conduction band remains unchanged and equals bulk InAs band gap in the unstrained case. This results in a very small change, $\approx 2\%$, of the effective QD e_1-h_1 gap when going from VBO=210 to 60 meV. Similarly, the different choice of a_v does not lead to significant change of the effective gap as overall InAs band-gap deformation potential $a_{gap}=a_c-a_v=-6.08$ eV is kept fixed for different values of a_v. The only notable difference in the gap prediction between Bir-Pikus and DFT models can be attributed to overestimation of conduction-band energies under biaxial strain, as mentioned previously. This difference emphasizes the importance of the proper modeling of strain in atomistic calculations and leaves open door for future research.

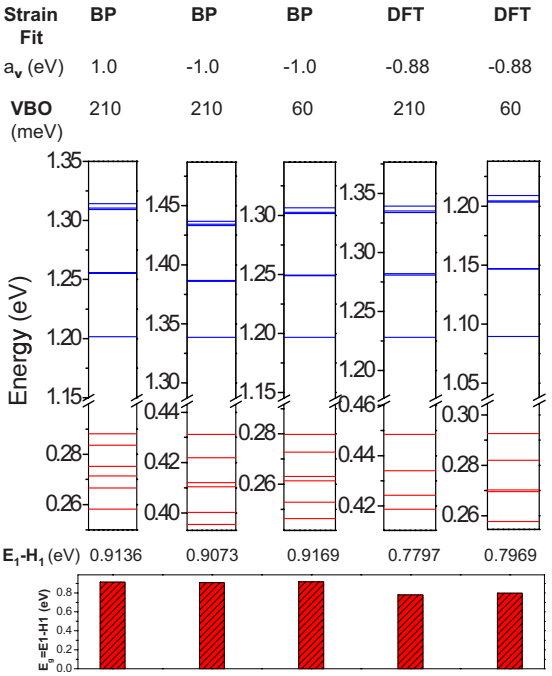

FIG. 3. (Color online) Electron (blue/upper/dark gray) and hole (red/lower/light gray) single-particle energies calculated for different values of InAs/GaAs VBO, different absolute (InAs) valence-band deformation potential a_v and different models, BP or DFT, used in fitting tight-binding Hamiltonian to reproduce strained bulk band edges.

As mentioned above, a_{gap} does not depend on the choice of a_v, however, different choice of a_v results in different value of absolute conduction-band deformation potential because $a_c=a_{gap}+a_v$, i.e., $a_c=-5.08$ or -7.08 eV, resulting in different energies of the ground electron level for different a_c. However, we note that general structure of electron levels remains fairly unchanged with well-pronounced shell structure and ground-first-excited-states spacing ≈ 50 meV for different choice of input parameters.

We also note here that structure of probability densities of confined electron states is very stable with respect to the choice of VBO and a_v parameters. For all cases considered in this work their charge density looks exactly the same as in Fig. 2, with the same nodal structure, elongation directions, and the spatial extent.

C. Dependence of valence hole levels on valence-band offset, deformation potential, and methodology

The detailed structure of hole states differs significantly with a different choice of input parameters. Figure 4 shows detailed probability density isosurfaces and energies for holes, calculated for different values of InAs/GaAs VBO, different absolute valence-band deformation potential a_v and different fitting targets, BP or DFT. The ground hole states

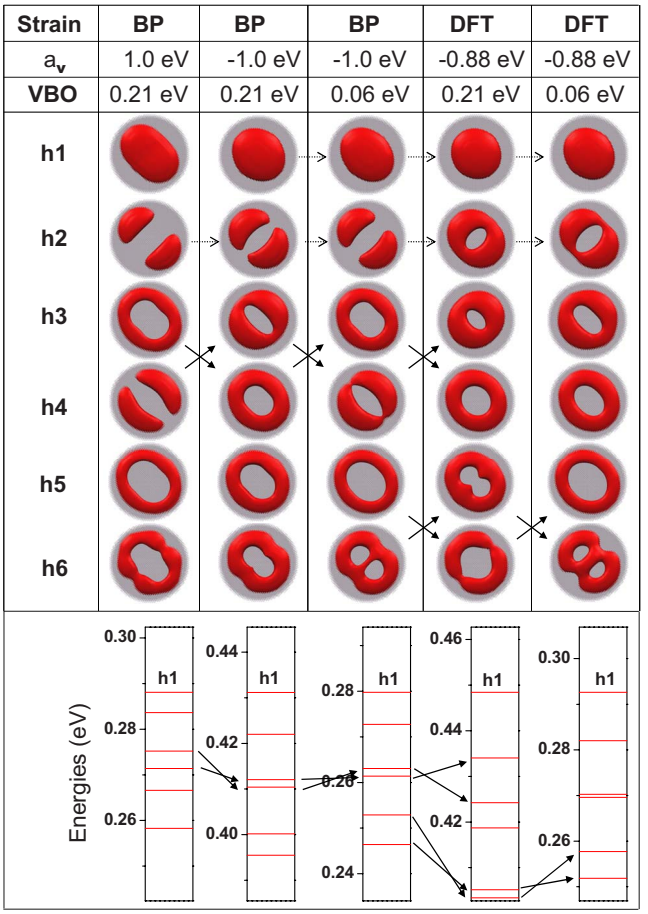

FIG. 4. (Color online) Hole probability density isosurfaces and energies calculated for different values of InAs/GaAs VBO, different absolute valence-band deformation potential a_v and different models, BP or DFT, used in fitting tight-binding Hamiltonian to reproduce strained bulk band edges.

remain of approximately s type, however, with different level of elongation depending on the model. Also, the first excited state is of p symmetry in all cases, localized along $[1\bar{1}0]$.

Higher lying states change their character and energy spacing depending on the choice of parameters, making it almost impossible to address the details of hole level structure without a better understanding of hole bulk properties: VBO and a_v. As these parameters are input to any atomistic calculation, we believe that similar uncertainties are present in results obtained by other authors.

To illustrate the problem, we show in Fig. 5 results of calculation for the same dot obtained with effective bond orbital method (EBOM),[41] tight-binding (TB) model with input parameters chosen similar to the ones used in empirical pseudopotential calculation (EMP1) from Ref. 15. Another empirical pseudopotential calculation (EMP2) is shown for comparison.[16]

As expected, the structure of electron states is similar in all cases, however, hole states differ significantly. EBOM maintains approximately a shell-like structure of hole levels. This differs from both TB and EMP and can be attributed to the replacement of zincblende with cubic symmetry in EBOM. There is a good agreement between

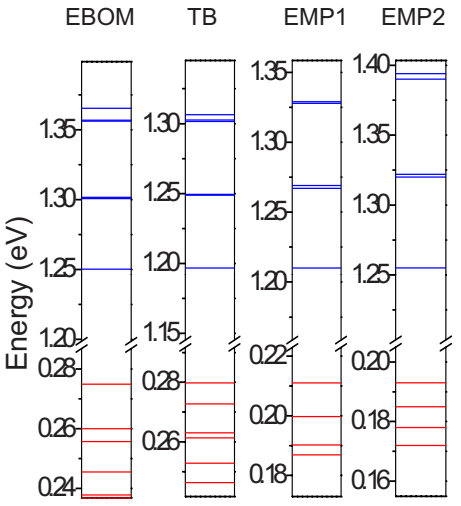

FIG. 5. (Color online) Electron (blue/upper/dark gray) and hole (red/lower/light gray) single-particle energies calculated for EBOM, TB model with parameters chosen similar to EMP1 from Ref. 15. Another EMP2 is shown for comparison from Ref. 16.

TB and EMP1 calculation, with a characteristic "large/large/small" level spacing between subsequent hole levels $h_1-h_2 \approx h_2-h_3 \gg h_3-h_4$.

Surprisingly, two pseudopotential (EMP1/EMP2) calculations predict different details of hole levels, most likely due to slightly different choice of fitting parameters or fitting results in pseudopotential fitting procedure. Figure 5 illustrates our point on importance of the choice of proper parametrization for all empirical atomistic calculations.

D. Single-particle optical properties

Symmetries of single-particle states directly influence quantum dot optical properties via the dipole moment matrix elements. Figure 6 shows joint optical density of states (single-particle absorption spectrum) calculated for light polarized along x axis ([100] crystal direction), i.e., $\langle \psi_{el}|x|\phi_{ho}\rangle$.

We observe three main groups of peaks corresponding to transitions between states from shells of similar symmetry,

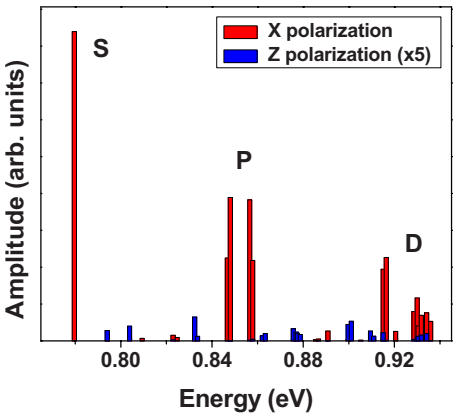

FIG. 6. (Color online) Joint optical density of states (single-particle absorption spectra) calculated for two light polarize along x (red/light gray) and z (blue/dark gray) axes.

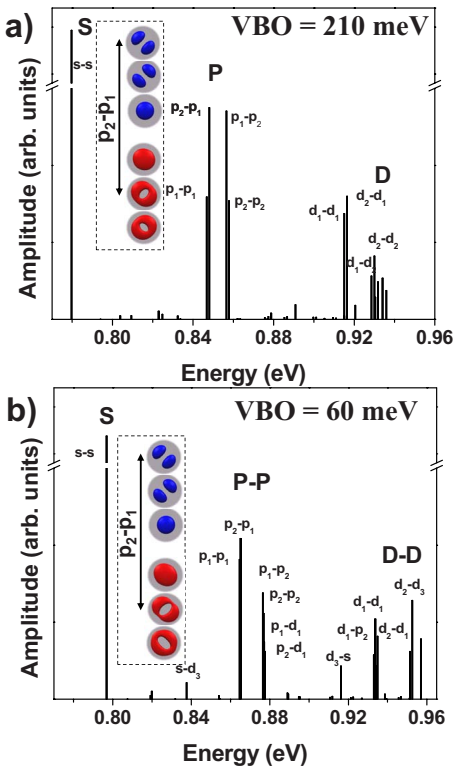

FIG. 7. (Color online) Joint optical density of states (single-particle absorption spectra) calculated for two different values of InAs/GaAs VBO (a) VBO=210 meV and (b) VBO=60 meV.

i.e., *s*-*s*, *p*-*p*, and *d*-*d*, with spacings among groups determined by spacing between *s*, *p*, and *d* electronic shells. However, as single-particle hole states are not purely *s*, *p*, or *d*, but rather of mixed angular momentum character, we also observe additional lines, not present in predictions of single-band effective-mass approximation. Figure 6 shows also that contribution from light polarized along *z* axis ([001]), i.e., growth direction, is negligible comparing to in-plane contribution, reflecting dominant confinement in *z* direction.

The atomistic character of underlying lattice, which results in inequivalency of crystal directions [110] and [1$\bar{1}$0] can also be observed in the optical spectrum. To quantify this effect we calculate the polarization ratio defined as

$$\lambda = \frac{P_{[110]}}{P_{[1\bar{1}0]}} = \frac{\langle \psi_{e1} | r_{[110]} | \psi_{h1} \rangle}{\langle \psi_{e1} | r_{[1\bar{1}0]} | \psi_{h1} \rangle}. \tag{15}$$

This ratio measures the difference in optical matrix elements for light polarization along different optical axis. For the system analyzed here, this ratio is equal 0.9 for the transition between ground electron and hole states. This is different from 1.0 for a system with full cylindrical symmetry.

As mentioned above, well-pronounced character of electron states and their stability with respect to different parameterizations enables us to label/classify hole states according to optical transitions to different electron states. Electron states e_2 and e_3 are of well-defined *p* character and we label them as p_1 and p_2 correspondingly. Similarly we label e_4, e_5, and e_6 as d_1, d_2, and d_3, respectively.

Figure 7 shows the comparison between joint optical density of states calculated for two different values of InAs/GaAs VBO: (a) VBO=210 meV and (b) VBO=60 meV. In both cases DFT model was used as a fitting target to describe the biaxial strain evolution with a_v=−0.88 as derived from DFT.

The overall blueshift in the VBO=60 meV case corresponds to larger effective gap. In both cases the characteristic splitting within the *p* shell reflects the splitting of the hole *p* shell ($h_3-h_2 \approx 10-12$ meV).

For VBO=210 meV allowed transitions occur only within a given shell (*s* to *s*, *p* to *p*, etc), which again allows us to classify h_2 and h_3 states as of *p* character and higher lying states as of mixed *d* character.

However, for VBO=60 meV, apart from the *p* to *p* transitions there are noticeable p_1-d_1 and p_2-d_1 lines corresponding to transitions from electronic *p* shell to hole $d_1(h_4)$ state and from electronic *d* shell to hole $p_2(h_3)$ state revealing mixed p/d character of h_3/h_4 states. This hybridization of states can also be expected from energy spectra, as these two states are very close in energy (Fig. 4). Notice that mixed character of states, well pronounced in JDOS, is not clearly visible in the charge-density distribution on Fig. 7, which emphasizes the usefulness of JDOS as a way of labeling QD states.

E. Many-body properties

Next we turn to calculating the many-body spectrum of the quantum dot.

1. Excitonic absorption spectrum

Figure 8 shows exciton absorption spectra calculated for two different values of InAs/GaAs VBO, (a) VBO=210 meV and (b) VBO=60 meV, using different levels of approximation in the many-body calculation.

First, in the single-particle (SP) picture all interactions between electron and hole states are neglected, SP being thus the joint optical density of states. Then, in the Hartree-Fock (HF) approximation only diagonal matrix elements of electron-hole Hamiltonian are included, corresponding effectively to a perturbative treatment of many-body effects. Finally, mixing between different configurations by Coulomb scattering is taken into account in a full configuration-interaction (CI) treatment.

First noticeable difference between different approximations is overall shift toward lower energies when going from (a) single particle to (b) "Hartree-Fock" case. This redshift is due to the attractive electron-hole Coulomb interaction equal 33.6 and 33.3 meV for VBO=210 and 60 meV correspondingly. Note that despite the 2% difference in the single-particle energy gap between two VBO cases the electron-hole Coulomb integral is almost identical.

The energy corresponding to the ground state of exciton is 746.1 meV (VBO=210 meV) and 763.5 meV (VBO=60 meV) and it is redshifted from the single-particle gap by electron-hole Coulomb interaction 33.6 and 33.3 meV for VBO=210 and 60 meV, respectively. In the CI case (c) the ground-state energy is further redshifted by the cor-

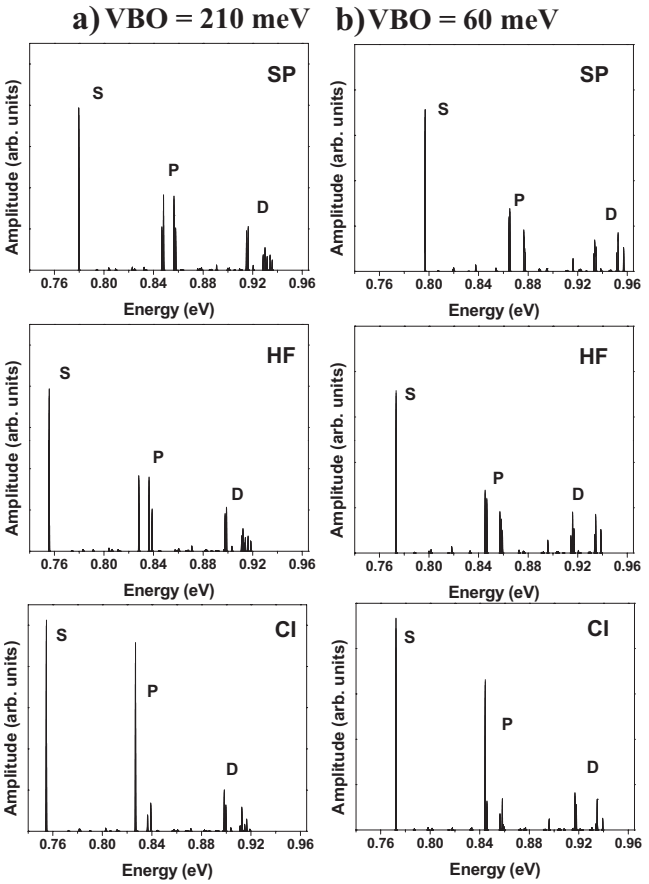

FIG. 8. Exciton absorption spectra calculated for two different values of InAs/GaAs VBO: (a) VBO=210 meV and (b) VBO=60 meV using different level of approximation in many-body calculation. First in SP picture all interactions between electron and hole are neglected, next in HF picture, only diagonal matrix elements of electron-hole Hamiltonian are included, finally mixing between different configurations (off diagonal, i.e., Coulomb scattering terms) is taken into account in full CI picture.

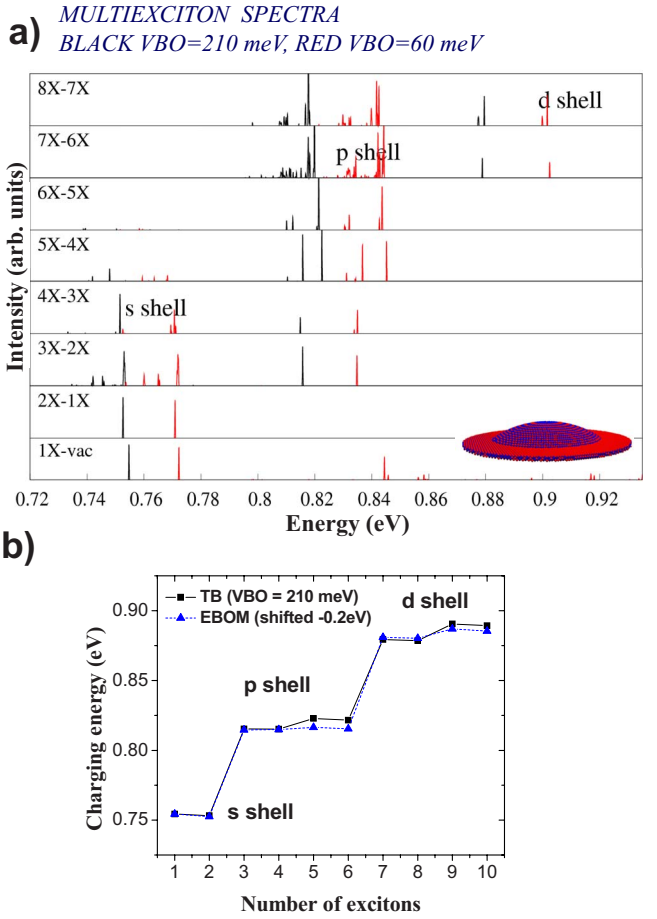

FIG. 9. (Color online) (a) Multiexciton emission spectra calculated for two different values of InAs/GaAs VBO: VBO=210 meV (black) and VBO=60 meV (red, light gray), (b) exciton charging energy as function of number of excitons.

rection due to correlation effects (≈1 meV).

Figure 8 also shows a quite significant difference in relative heights of absorption lines, when going from (a) to (c). Surprisingly, some of the noticeable differences between VBO=210 and 60 meV visible in initial single-particle properties are smeared out by interactions in the final, fully correlated calculation. These two observations stress out the necessity of full many-body treatment of excitonic effects in quantum dots. Interestingly, the excitonic absorption spectra comprising of a single "*s*" shell and dominant "*p*" shell absorption peaks seem to compare very well with absorption spectra predicted from the effective-mass model.[42]

2. Multiexciton complexes

Finally, we analyze the spectrum of multiexciton complexes. As already mentioned, the lens-type quantum dot shows only quasidegenerate electronic shells for the electron states with hole states being more complicated, without a clear shell structure. However, as we could see above in the exciton absorption spectra, the optical properties of QDs including many-body effects are still dominated by the single-particle spacings of the electron states *s*, *p*, etc.

Figure 9 shows the emission spectra from the multiexciton complexes as a function of the number of excitons, showing filling of quasidegenerate shells. In other words, Fig. 9 presents recombination spectra of an electron-hole pair in the presence of several other electron-hole pairs. Namely, for the 3*X* complex we show emission spectra of the electron-hole pair recombing in the presence of two other electron-hole pairs, etc. We see well-defined groups of peaks belonging to *s*, *p*, and *d* approximate shells. We see also that the emission from the *s*, *p*, and *d* shells is not a sensitive function of the number of excitons as postulated by "hidden symmetry" arguments.[43–45] The small structure of the *p* shell emission (for 3*X* and 4*X*) is related to the total spin and scattering to higher shells, while more complicated *p* shell emission for the 5*X* and 6*X* complexes is related to the splitting of the hole *p* states. The associated emission structure in the *s* shell energy range is not related to hidden symmetries and is a sensitive function of the filling of the shell, in agreement with results obtained using the effective-mass harmonic oscillator states.[44]

Figure 9(b) shows the exciton charging spectrum, defined as the energy needed to add one exciton to a system already

containing N excitons. Despite the complicated structure of hole levels, the charging spectra also reveal well-defined steps corresponding to filling of subsequent shells. However, a comparison with EBOM (Ref. 5) (shifted by −0.2 eV to match the energy of ground the exciton states) shows a small step for the case of $5X$ and $9X$ due to the splitting of the hole p and d states.

When the fifth (ninth) hole is added to the system it has to occupy the second of the p states (third of the d states) due to the Pauli exclusion principle. Due to the splitting in hole spectrum this state has a different single-particle energy resulting in a step in charging spectrum.

XI. CONCLUSIONS

We presented here an atomistic $sp^3d^5s^*$ tight-binding theory of electronic structure and optical properties of InAs/GaAs self-assembled quantum dots. The atomistic theory includes zincblende symmetry, faceting, and atomic orbitals accounting for interband and intervalley couplings. The equilibrium position of atoms is calculated using the valence force field (VFF) method and modification of the tight-binding Hamiltonian due to strain is accounted for using Harrison's law. The electronic and optical properties of multiexciton complexes are determined by solving the many-body Hamiltonian for interacting electrons and holes using the configuration-interaction approach. The methodology is applied to an InAs/GaAs lens-shaped quantum dot. The dependence of calculated electron and hole electronic states on the InAs/GaAs valence-band offsets and InAs absolute valence-band deformation potentials is described. It is shown that the electron levels are well described by the effective-mass harmonic oscillator model. The hole levels are found not to have a well-defined shell structure, and their levels are found to be sensitive to the choice of the valence-band offset and valence-band dependence on strain, i.e., parameters which are not well known. Given the set of bulk parameters, the reliability of the atomistic calculations was positively assessed by comparison with results of the empirical pseudopotentials method and effective bond orbital method. Future work will address the structure of valence holes by comparison with available experiments. In the end, this will establish tight-binding methodology as a useful tool in designing semiconductor nanostructures starting with their atomic constituents and ending with their electronic and optical properties.

ACKNOWLEDGMENTS

The authors acknowledge useful discussions with G. Bryant, H. Guo, and G. Klimeck and support from the Canadian Institute for Advanced Research, QuantumWorks, NRC-NSERC-BDC Nanotechnology Projects and NSERC. M. Zielinski acknowledges the financial support of the Future and Emerging Technologies (FET) programme within the Seventh Framework Programme for Research of the European Commission, under the FET-Open grant agreement CORNER No. FP7–ICT-213681. We thank W. Sheng for providing the results of EBOM calculations and E. Kadantsev for DFT simulations.

*Present address: Instytut Fizyki UMK, Grudziądzka 5, 87-100 Toruń, Poland.

[1] P. Hawrylak and M. Korkusinski, in *Single Quantum Dots: Fundamentals, Applications, and New Concepts*, Topics in Applied Physics Vol. 90, edited by P. Michler (Springer, New York, 2003.
[2] L. Jacak, P. Hawrylak, and A. Wojs, *Quantum Dots* (Springer, Berlin, 1998).
[3] D. Bimberg, M. Grundmann, and N. N. Ledentsov, *Quantum Dot Heterostructures* (Wiley, New York, 1998).
[4] C. D. Spataru, S. Ismail-Beigi, L. X. Benedict, and S. G. Louie, Phys. Rev. Lett. **92**, 077402 (2004).
[5] W. Sheng, S.-J. Cheng, and P. Hawrylak, Phys. Rev. B **71**, 035316 (2005).
[6] W. Sheng and P. Hawrylak, Phys. Rev. B **72**, 035326 (2005).
[7] S. Schulz, S. Schumacher, and G. Czycholl, Phys. Rev. B **73**, 245327 (2006).
[8] S. Lee, L. Jönsson, J. W. Wilkins, G. W. Bryant, and G. Klimeck, Phys. Rev. B **63**, 195318 (2001).
[9] K. Leung and K. B. Whaley, Phys. Rev. B **56**, 7455 (1997).
[10] R. Santoprete, Belita Koiller, R. B. Capaz, P. Kratzer, Q. K. K. Liu, and M. Scheffler Phys. Rev. B **68**, 235311 (2003).
[11] M. Korkusinski, M. Zielinski, and P. Hawrylak, J. Appl. Phys. **105**, 122406 (2009).
[12] W. Jaskólski, M. Zieliński, G. W. Bryant, and J. Aizpurua, Phys. Rev. B **74**, 195339 (2006).
[13] A. Canning, L. W. Wang, A. Williamson, and A. Zunger, J. Comput. Phys. **160**, 29 (2000).
[14] G. Bester and A. Zunger, Phys. Rev. B **71**, 045318 (2005).
[15] L. He and A. Zunger, Phys. Rev. B **73**, 115324 (2006).
[16] A. J. Williamson, L. W. Wang, and A. Zunger, Phys. Rev. B **62**, 12963 (2000).
[17] G. Klimeck, R. C. Bowen, T. B. Boykin, and T. A. Cwik, Superlattices Microstruct. **27**, 519 (2000).
[18] T. B. Boykin, G. Klimeck, R. C. Bowen, and F. Oyafuso, Phys. Rev. B **66**, 125207 (2002).
[19] P. R. C. Kent, G. L. W. Hart, and A. Zunger, Appl. Phys. Lett. **81**, 4377 (2002).
[20] C. Pryor, J. Kim, L. W. Wang, A. J. Williamson, and A. Zunger, J. Appl. Phys. **83**, 2548 (1998); M. Tadić, F. M. Peeters, K. L. Janssens, M. Korkusinski, and P. Hawrylak, *ibid.* **92**, 5819 (2002).
[21] P. N. Keating, Phys. Rev. **145**, 637 (1966); R. M. Martin, Phys. Rev. B **1**, 4005 (1970).
[22] S. Lee, F. Oyafuso, P. von Allmen, and G. Klimeck, Phys. Rev. B **69**, 045316 (2004).
[23] D. J. Chadi, Phys. Rev. B **16**, 790 (1977).
[24] J. C. Slater and G. F. Koster, Phys. Rev. **94**, 1498 (1954).
[25] P. Vogl, H. P. Hjalmarson, and J. D. Dow, J. Phys. Chem. Solids **44**, 365 (1983).
[26] J. M. Jancu, R. Scholz, F. Beltram, and F. Bassani, Phys. Rev. B

57, 6493 (1998).
[27] J. G. Díaz and G. W. Bryant, Phys. Rev. B **73**, 075329 (2006).
[28] W. A. Harrison, *Electronic Structure and the Properties of Solids* (Freeman, New York, 1980).
[29] G. L. Bir and G. E. Pikus, *Symmetry and Strain-Induced Effects in Semiconductors* (Wiley, New York, 1974).
[30] S. H. Wei and A. Zunger, Phys. Rev. B **60**, 5404 (1999).
[31] Y. H. Li, X. G. Gong, and S. H. Wei, Phys. Rev. B **73**, 245206 (2006).
[32] Chris G. Van de Walle, Phys. Rev. B **39**, 1871 (1989).
[33] E. Kadantsev (unpublished).
[34] M. Korkusinski and M. Zielinski (unpublished).
[35] I. Vurgaftman, J. R. Meyer, and W. L. R. Ram-Mohan, Appl. Phys. Rev. **89**, 5815 (2001).
[36] C. G. Van de Walle and J. Neugebauer, Nature (London) **423**, 626 (2003).
[37] S. V. Goupalov and E. L. Ivchenko, Phys. Solid State **43**, 1867 (2001).
[38] G. W. Bryant and W. Jaskólski, Phys. Rev. B **67**, 205320 (2003).
[39] Z. R. Wasilewski, S. Fafard, and J. P. McCaffrey, J. Cryst. Growth **201-202**, 1131 (1999).
[40] S. Raymond, S. Studenikin, A. Sachrajda, Z. Wasilewski, S. J. Cheng, W. Sheng, P. Hawrylak, A. Babinski, M. Potemski, G. Ortner, and M. Bayer, Phys. Rev. Lett. **92**, 187402 (2004).
[41] W. Sheng (unpublished).
[42] P. Hawrylak, G. A. Narvaez, M. Bayer, and A. Forchel, Phys. Rev. Lett. **85**, 389 (2000).
[43] A. Wojs and P. Hawrylak, Solid State Commun. **100**, 487 (1996).
[44] P. Hawrylak, Phys. Rev. B **60**, 5597 (1999).
[45] P. Hawrylak, Solid State Commun. **127**, 753 (2003).